
Robust Hyperbolic Learning with Curvature-Aware Optimization

Ahmad Bdeir^{*1} Johannes Burchert² Lars Schmidt-Thieme² Niels Landwehr¹

Abstract

Hyperbolic deep learning has become a growing research direction in computer vision due to the unique properties afforded by the alternate embedding space. The negative curvature and exponentially growing distance metric provide a natural framework for capturing hierarchical relationships between datapoints and allowing for finer separability between their embeddings. However, current hyperbolic learning approaches are still prone to overfitting, computationally expensive, and prone to instability, especially when attempting to learn the manifold curvature to adapt to tasks and different datasets. To address these issues, our paper presents a derivation for Riemannian AdamW that helps increase hyperbolic generalization ability. For improved stability, we introduce a novel fine-tunable hyperbolic scaling approach to constrain hyperbolic embeddings and reduce approximation errors. Using this along with our curvature-aware learning schema for Lorentzian Optimizers enables the combination of curvature and non-trivialized hyperbolic parameter learning. Our approach demonstrates consistent performance improvements across Computer Vision, EEG classification, and hierarchical metric learning tasks achieving state-of-the-art results in two domains and drastically reducing runtime.

1. Introduction

Recently, hyperbolic manifolds have gained attention in deep learning for their ability to model hierarchical and tree-like data structures efficiently. Unlike Euclidean space, hyperbolic space has negative curvature, allowing it to represent exponentially growing distances. This makes these manifolds ideal for tasks like natural language processing, graph representation, and recommendation systems (Peng

et al., 2022). By embedding data into hyperbolic space, models can capture complex relationships more effectively, often with fewer parameters (Ganea et al., 2018), leading to improved performance and interpretability. Hyperbolic geometry has also found applications in computer vision, where its ability to better separate embeddings in high-dimensional spaces has shown promise in improving tasks like image classification and segmentation (Bdeir et al., 2024; van Spengler et al., 2023; Khruikov et al., 2020; Atigh et al., 2022), few-shot learning (Liu et al., 2020), and feature representation (Yang et al., 2023).

Two main derivations of hyperbolic space have emerged as learning frameworks: the hyperboloid or the Lorentz space (\mathbb{L}) and the Poincaré manifold (\mathbb{P}). Typically, the hyperboloid, or Lorentz space, offers better operational stability, as demonstrated by Mishne et al. (2022) but lacks clear definitions for basic vector operations such as addition and subtraction. To bridge this gap, recent research has focused on defining Lorentzian versions of common deep learning operations, such as the feed-forward layer (Chen et al., 2022; Dai et al., 2021; Ganea et al., 2018), convolutional layer (Chen et al., 2022; Qu & Zou, 2023; Dai et al., 2021), and MLRs (Bdeir et al., 2024).

However, the use of these hyperbolic operations comes with challenges. Computations in hyperbolic space are more complex and expensive due to the increased mathematical complexity and the lack of optimized CUDA implementations, which can slow down training and drastically increase memory requirements. Additionally, optimization on hyperbolic manifolds can be unstable, especially in low floating-point precision environments. This has required research to rely on parameter clamping techniques, which can cause non-smooth gradient updates, to remain within the accurate representation radius for manifolds (Mishne et al. (2022); Guo et al. (2022)). Otherwise, performance either suffers or training becomes impossible due to the precision errors causing mathematically undefined operations. The instability is only exacerbated when we incorporate the negative curvature as a learned parameter since it directly affects the representational radius and requires the projection of vectors between these different curved manifolds. Finally, in data-scarce scenarios, the higher representational capacity makes the hyperbolic spaces more prone to overfitting which heavily impacts their generalization ability.

¹Department of Data Analytics, University of Hildesheim, Germany ²The Information Systems and Machine Learning Lab, University of Hildesheim, Germany. Correspondence to: Ahmad Bdeir <Bdeira@uni-hildesheim.de>, Johannes Burchert <burchert@ismll.de>.

This work addresses key challenges in the Lorentz model. To combat overfitting, we introduce an AdamW-based optimizer that enhances regularization and generalization in hyperbolic learning. For learning instability, we propose an optimization framework that stabilizes curvature parameter learning. We also present a smoother scaling function to replace weight clipping, ensuring hyperbolic vectors remain within the representational radius. To tackle computational complexity, we introduce an implementation trick that leverages efficient CUDA-based convolutions for hyperbolic learning. Improved stability not only boosts model performance but also enables lower-precision training, enhancing efficiency. Our contributions are four-fold:

1. We propose a formulation for Riemannian AdamW and an alternative schema for Riemannian optimizers that stabilize curvature learning for hyperbolic parameters.
2. We propose the use of our maximum distance rescaling function to restrain hyperbolic vectors within the representative radius of accuracy afforded by the number precision, even allowing for fp16 precision.
3. We present *HCNN+*, *HyperMAtt*, and *LHEIR*, an application of our proposed optimization scheme for the domains of classical image classification, EEG classification, and hierarchical metric learning respectively.
4. We empirically show the effectiveness of our proposed methods in three domains, hierarchical metric learning, Image, and EEG classification, where we achieve state-of-the-art performance in two domains with a significant computational speed-up.

Our code is publicly available at [redacted for double-blind submission].

2. Related Work

Hyperbolic Embeddings in Deep Learning With the success of employing hyperbolic manifolds in NLP models (Zhu et al., 2021; Dhingra et al., 2018; Tifrea et al., 2018) hyperbolic embeddings have extended to the computer vision domain. Initially, many of the works relied on a hybrid architecture, utilizing Euclidean encoders and hyperbolic decoders (Mettes et al., 2023). This was mainly due to the high computational cost of hyperbolic operations in the encoder, as well as the lack of well-defined alternatives for Euclidean operations. However, this trend has begun to shift towards the utilization of fully hyperbolic encoders as can be seen in the hyperbolic Resnets by Bdeir et al. (2024) and van Spengler et al. (2023). Both works offer hyperbolic definitions for 2D convolutional layer, batch normalization layer, and an MLR for the final classification head. Bdeir

et al. (2024) even attempt to hybridize the encoder by employing the Lorentz manifold in blocks that exhibit higher output hyperbolicity. While this has led to notable performance improvements, both models suffer from upscaling issues. Attempting to replicate these approaches for larger datasets or bigger architectures becomes much less feasible in terms of time and memory requirements. Instead, our approach places higher focus on efficient components to leverage the beneficial hyperbolic properties of the model while minimizing the memory and computational footprint.

Curvature Learning Previous work in hyperbolic spaces has explored various approaches to curvature learning. In their studies, Gu et al. (2018) and Giovanni et al. (2022) achieve this by using a radial parametrization that implicitly models variable curvature embeddings under an explicitly defined, fixed 1-curve manifold. This method enables them to simulate K-curve hyperbolic and spherical operations under constant curvature for the mixed-curve manifold specifically, a combination of the Euclidean, spherical, and Poincaré manifold. Other approaches, such as the one by Kochurov et al. (2020), simply set the curvature to a learnable parameter but do not account for the manifold changes in the Riemannian optimizers. This leads to hyperbolic vectors being updated with mismatched curvatures and others being inaccurately reprojected, resulting in instability and accuracy degradation. Additionally, some methods, like the one by Kim et al. (2023), store all manifold parameters as Euclidean vectors and project them before use. While this approach partially mitigates the issue of mismatched curvature operations, it remains less accurate and more computationally expensive. In comparison, our proposed optimization schema maintains the parameters on the manifold and optimizes them directly by performing the necessary operations to transition between the variable curvature spaces.

3. Methodology

3.1. The Lorentz Space

The hyperbolic space is a Riemannian manifold with a constant negative sectional curvature $c < 0$. There are many conformal models of hyperbolic space but we focus our work on the hyperboloid, or Lorentz manifold. The n -dimensional Lorentz model $\mathbb{L}_K^n = (\mathcal{L}^n, \mathfrak{g}_x^K)$ is defined with $\mathcal{L}^n := \{\mathbf{x} = [x_t, \mathbf{x}_s] \in \mathbb{R}^{n+1} \mid \langle \mathbf{x}, \mathbf{x} \rangle_{\mathcal{L}} = \frac{-1}{K}, x_t > 0\}$ where $\frac{-1}{K} = c$ and the Lorentzian inner product as Riemannian metric $\mathfrak{g}_x^K = \langle \mathbf{x}, \mathbf{y} \rangle_{\mathcal{L}} := -x_t y_t + \mathbf{x}_s^T \mathbf{y}_s$. It then follows that $\langle \mathbf{x}, \mathbf{y} \rangle_{\mathcal{L}} < \frac{-1}{K}$ which is an important characteristic to note for the stability issues presented later on. The formulation \mathcal{L}^n then presents the Lorentz manifold as the upper sheet of a two-sheeted hyperboloid centered at $\bar{0} = [\sqrt{K}, 0, \dots, 0]^T$.

We inherit the terminology of special relativity and refer to the first dimension of a Lorentzian vector as the time component x_t and the remainder of the vector, as the space dimension \mathbf{x}_s . Below are the basic operations presented by the manifold with more complex operations provided in Appendix A.

Distance Distance in hyperbolic space is the magnitude of the geodesic forming the shortest path between two points. Let $\mathbf{x}, \mathbf{y} \in \mathbb{L}_K^n$, the distance between them is given by

$$d_{\mathbb{L}}(\mathbf{x}, \mathbf{y}) = \sqrt{K} \cosh^{-1}\left(\frac{-\langle \mathbf{x}, \mathbf{y} \rangle_{\mathbb{L}}}{K}\right) \quad (1)$$

We also define the square distance by Law et al. (2019) as $d_{\mathbb{L}}^2(\mathbf{x}, \mathbf{y}) = \|\mathbf{x} - \mathbf{y}\|_{\mathbb{L}}^2 = -2K - 2\langle \mathbf{x}, \mathbf{y} \rangle_{\mathbb{L}}$.

Exponential and Logarithmic Maps Since the Lorentz space is a Riemannian manifold, it is locally Euclidean. This can best be described through the tangent space $\mathbb{T}_{\mathbf{x}}\mathcal{M}$, a first-order approximation of the manifold at a given point \mathbf{x} . The exponential map, $\exp_{\mathbf{x}}^K(\mathbf{z}) : \mathbb{T}_{\mathbf{x}}\mathbb{L}_K^n \rightarrow \mathbb{L}_K^n$ is then the operation that maps a tangent vector $\mathbb{T}_{\mathbf{x}}\mathbb{L}_K^n$ onto the manifold through $\exp_{\mathbf{x}}^K(\mathbf{z}) = \cosh(\alpha)\mathbf{x} + \sinh(\alpha)\frac{\mathbf{z}}{\alpha}$, with $\alpha = \sqrt{1/K}\|\mathbf{z}\|_{\mathbb{L}}$, $\|\mathbf{z}\|_{\mathbb{L}} = \sqrt{\langle \mathbf{z}, \mathbf{z} \rangle_{\mathbb{L}}}$. The logarithmic map is the inverse of this mapping and can be described as $\log_{\mathbf{x}}^K(\mathbf{y}) = \frac{\cosh^{-1}(\beta)}{\sqrt{\beta^2-1}} \cdot (\mathbf{y} - \beta\mathbf{x})$, with $\beta = -\frac{1}{K}\langle \mathbf{x}, \mathbf{y} \rangle_{\mathbb{L}}$.

3.2. Riemannian Optimization Schema

Background In the GeoOpt hyperbolic learning library, Kochurov et al. (2020) introduces the curvature c of hyperbolic space as a learnable parameter. However, no subsequent work has fully taken advantage of this feature despite the authors presenting ready implementations of hyperbolic operations that account for this curvature. Our empirical testing also reveals that naively learning this parameter often leads to instability and performance decline. We attribute these issues to the simplistic curvature updates in Riemannian optimizers, which neglect to adjust hyperbolic operations, weights, and gradients after updating the curvature.

In the current Riemannian optimization approach, Euclidean gradients and momentums are projected onto the manifold to update hyperbolic parameters. However, since optimization depends on curvature, adjusting it during learning makes previous projections, gradients, and parameters inconsistent with the new geometry. Essentially, the current schema applies updates using the new curvature on vectors defined by the old curvature, leading to mismatches.

To illustrate this, Figure 1 shows two manifolds with different curvatures. It is evident that points defined on the first manifold do not lie on the second, and the tangent planes of the first manifold are not aligned with those of the second.

Thus, using the new curvature operations on points from the old model is not mathematically sound practice. This inconsistency introduces instability, undermining the reliability of curvature learning and often leading to undefined values during the parameter updates.

One example of this is the distance function Equation (1) which requires the bound $\langle \mathbf{x}, \mathbf{y} \rangle_{\mathbb{L}} < \frac{-1}{K}$ to hold. If the new curvature parametrization at time t $K_t > K_{t-1}$ then the input into the inverse hyperbolic cosine has a lower bound less than 1, leaving room for the operation to be mathematically undefined.

While GeoOpt does not address this particular optimization challenge, it does implement an "N-stabilize step". This step aims to reduce instability by recalculating the time component of the hyperbolic parameters every N-steps to ensure they remain on the manifold. However, this approach is done after the update step and does not prevent invalid parameter values during optimization.

Curvature Aware Optimization To address this, we propose a method that tracks both the old and new curvature parameter values θ_K throughout updates. Specifically, we propose a simple approach where all updates are first applied under the old curvature, then the new curvature is derived and finally, the hyperbolic vectors are mapped from the old manifold to the new one.

The previously proposed mapping technique in the N-stabilize step alters the relative magnitudes of the hyperbolic parameters $\theta_{\mathbb{L}}$ and gradients \mathcal{G} , as well as the directions of the momentums, which can degrade performance and lead to training instability. Instead, we recommend projecting points onto the tangent space at the origin of the old curvature $\bar{\mathbf{0}}_{t-1}$ using the logarithmic map and then projecting back after the curvature update. Gradients and their momentum can be similarly projected or parallel transported (Appendix A) to the tangent space. The entire optimization schema can then be seen in Algorithm 1.

Here, we choose to apply parallel transport, or any similar approximation of it, because it preserves the gradient vectors' directions which is important for the optimization procedure. We also choose to use the tangent space at the origin as the mapping intermediate since it remains relatively stable when the curvature is updated, as shown in Figure 1. Finally, we prove that the vector norms and their hyperbolic distances to the origin are preserved since $D(\exp_{\bar{\mathbf{0}}}^{K_1}(\mathbf{y}), \bar{\mathbf{0}})^{K_1} = \|\mathbf{y}\| = D(\exp_{\bar{\mathbf{0}}}^{K_2}(\mathbf{y}), \bar{\mathbf{0}})^{K_2}$ where $\mathbf{y} \in \mathcal{T}_{\bar{\mathbf{0}}}\mathcal{M}$.

It is important to emphasize that our proposed optimization scheme is compatible with existing curvature learning and meta-learning methods. Rather than being an alternative, it serves as a guideline for updating manifold parameters

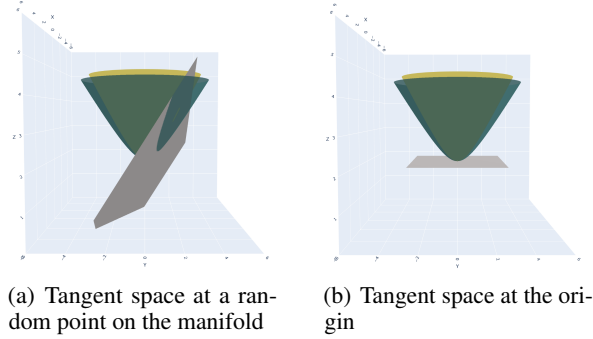


Figure 1: Tangent planes of a hyperboloid with curvature -1 relative to another hyperboloid with curvature -0.7. Tangential properties between manifolds are better respected at the origin where tangents remain parallel.

during curvature changes, aimed at maintaining learning stability throughout the process.

3.3. Riemannian AdamW Optimizer

Background The AdamW optimizer was first introduced by Loshchilov & Hutter (2019) and relies on an improved application of the L2-regularization factor in the base Adam optimizer. L2-regularization works on the principle that networks with smaller weights tend to have better generalization performance than equal networks with higher weight values. Adam applied the L2-regularization during the gradient update step by incorporating it in the loss. However, Loshchilov & Hutter (2019) argue that this is inconsistent since the regularization effect is reduced by the magnitude of the gradient norms. Instead, they apply the weight decay directly during the parameter update step. AdamW is then shown to generalize better and lead to better convergence and has become a popular choice for many vision tasks.

Given the above, we believe AdamW is significant for hyperbolic learning. Hyperbolic spaces, with their higher representational capacity, are prone to overfitting, especially under data scarcity during training (Gao et al., 2022). Thus, AdamW’s enhanced L2-regularization could improve hyperbolic models.

Riemannian AdamW In the following, we derive AdamW for the Lorentz manifold and suggest its extension to the Poincaré ball. The key difference between AdamW and Riemannian Adam lies in direct weight regularization, which is challenging in Lorentz space due to the lack of an intuitive subtraction operation. To address this, we re-frame parameter regularization in AdamW as a weighted centroid with the origin $\bar{\mathbf{0}}$

$$\boldsymbol{\theta}_{t-1} - \gamma\lambda\boldsymbol{\theta}_{t-1} = (1 - \gamma\lambda)\boldsymbol{\theta}_{t-1} + \gamma\lambda\bar{\mathbf{0}}$$

where γ is the learning rate and λ is the weight decay value.

Algorithm 1 Curvature Learning Aware Optimization

Given parameters $\boldsymbol{\theta} = [\boldsymbol{\theta}_{euclid}, \boldsymbol{\theta}_{\mathbb{L}}, \boldsymbol{\theta}_K]$ and gradients denoted \mathcal{G}

function Optimizer Step

for p in $\boldsymbol{\theta}_{\mathbb{L}}$ **do**

 Vanilla Riemannian Optimizer Step

end for

for p in $\boldsymbol{\theta}_{euclid} \cup \boldsymbol{\theta}_K$ **do**

 Vanilla Euclidean Optimizer Step

end for

 MoveParameters()

end function

function Move Parameters

for p in $\boldsymbol{\theta}_{\mathbb{L}}$ **do**

$\mathcal{G}_{temp} = \text{PT}_{p \rightarrow \bar{\mathbf{0}}_{t-1}}^{K_{t-1}}(\mathcal{G})$

$z = \log_{\bar{\mathbf{0}}_{t-1}}^{K_{t-1}}(p)$

$p = \exp_{\bar{\mathbf{0}}_t}^{K_t}(z)$

$\mathcal{G} = \text{PT}_{\bar{\mathbf{0}}_t \rightarrow p}^{K_t}(\mathcal{G}_{temp})$

end for

end function

The centroid operation is well defined in the Lorentz space which now allows for a direct translation of AdamW. The regularization schema becomes:

$$\boldsymbol{\theta}_t = \begin{cases} \mu_{\mathbb{L}}([\boldsymbol{\theta}_{t-1}, \bar{\mathbf{0}}], \boldsymbol{\nu} = [1 - \gamma\lambda, \gamma\lambda]) & \text{if } \boldsymbol{\theta} \in \mathbb{L} \\ \boldsymbol{\theta}_{t-1} - \gamma\boldsymbol{\theta}_{t-1}\lambda & \text{otherwise} \end{cases}$$

where $\mu_{\mathbb{L}}$ is the Lorentz centroid, and $\boldsymbol{\nu}$ are the weights. By removing the later gradient decay and introducing this operation, we adapt AdamW for use in the Lorentz space.

3.4. Maximum Distance Rescaling

Background Vectors in the hyperboloid models can be defined as $\mathbf{x} = [x_t, \mathbf{x}_s]^T \in \mathbb{L}_K^n$ where $x_t = \sqrt{\|\mathbf{x}_s\|^2 + K}$, $K = -1/c$ and c is the manifold curvature. As such, Lorentzian projections and operations rely on the ability to accurately calculate the corresponding time component x_t for the hyperbolic vectors. Under Float64 precision, Mishne et al. (2022) derive a maximum value for the time component $x_{t_{max}} = 10^8$. Values above this push vectors off the Lorentz manifold and onto the cone defined by $x_t^2 = \sum \mathbf{x}_s^2$. As an example for sources of instability, we reference again the inner product in the distance function in Equation (1), where the approximations can lead to undefined mathematical values by pushing the inverse hyperbolic cosine input to less than one. Based on the above, and given a specific K , we can derive a maximum representational radius for the model as

$$D_{\mathbf{0}_{max}}^K = \operatorname{arccosh}\left(\frac{x_{t_{max}}}{\sqrt{K}}\right) \cdot \sqrt{K} \quad (2)$$

Under Float32 precision, and to account for values of $K < 1$ we use a limit value of $x_{t_{max}} = 2 \cdot 10^3$. When projected onto the tangent space of the origin, and with $K = 1$, this translates to $\|\log_{\mathbf{0}}^1(\mathbf{x})\| = D_{\mathbf{0}_{max}}^1 = 9.1$. This value changes considerably as the value of K changes. Vectors outside this radius lead to instability and performance degradation due to inaccurate approximation. This problem is only exacerbated as the dimensionality of the hyperbolic vector increases. Higher dimensional vectors tend to have larger norms which limits hyperbolic models' abilities to scale up.

To constrain hyperbolic vectors within a specified maximum distance, either a normalization function or a parameter clipping method is required. Parameter clipping can be challenging to train, as it may lead to information loss and introduce non-smooth gradients. On the other hand, common normalization functions like tanh and the sigmoid function tend to saturate quickly, limiting their effectiveness as seen in the sigmoid implementation by Chen et al. (2022).

Flexible Scaling Function To address these issues, we introduce a modified scaling function, designed to provide finer control over both the maximum values and the slope of the curve. A visualization of this function is provided in Figure 2, and the formulation is presented below:

$$\mathbf{y}_{rescaled} = \frac{\mathbf{y}}{\|\mathbf{y}\|} \cdot m \cdot \tanh\left(\|\mathbf{y}\| \cdot \frac{\operatorname{atanh}(0.99)}{s \cdot m}\right) \quad (3)$$

where $y \in \mathbb{R}^d$, m is our desired maximum value, and s controls the slope of the curve. We now have a maximum distance value to adhere to and a flexible distance normalizing function. To apply this to the hyperbolic vectors, we

suggest performing the scaling on the tangent plane of the origin. However, this is an expensive operation to perform repeatedly, as such we derive in Appendix C the equivalent factorized form for the scaling of the space values:

$$\mathbf{x}_{s_{rescaled}} = \mathbf{x}_s \times \frac{e^{\frac{D(\mathbf{x}, \mathbf{0})_{rescaled}^K}{\sqrt{K}}} - e^{-\frac{D(\mathbf{x}, \mathbf{0})_{rescaled}^K}{\sqrt{K}}}}{e^{\frac{D(\mathbf{x}, \mathbf{0})^K}{\sqrt{K}}} - e^{-\frac{D(\mathbf{x}, \mathbf{0})^K}{\sqrt{K}}}} \quad (4)$$

where $D(\mathbf{x}, \mathbf{0})_{rescaled}^k$ is the scaled distances by plugging in $D(\mathbf{x}, \mathbf{0})$ and $D_{\mathbf{0}_{max}}^K$ in Equation (3). The time component of the vector is recalculated based on the norm of its spatial components, providing a complete scaling operation for the Lorentz space. We apply this tanh scaling during transitions between manifolds, including from Euclidean to Lorentz spaces and between Lorentz spaces of different curvatures. It is also used after Lorentz Boosts and direct Lorentz concatenations (Qu & Zou, 2022), as well as following variance-based rescaling in the batch normalization layer, where adjustments can push points outside the valid radius, often resulting in invalid values.

4. Domain Adaption

In order to empirically prove the effectiveness of our proposed solutions, we apply them to metric learning, EEG classification, image classification, and image generation tasks. In the following, we tackle each of these tasks by offering a brief overview of the problem setting with an existing reference model, our hyperbolic adaptation for this problem, and the goal from this experimental setup.

4.1. Hierarchical Metric Learning Problem

Problem Setting and Reference Model In their paper Kim et al. (2023) take on the problem of hierarchical clustering using an unsupervised hyperbolic loss regularizer they name HIER. This method relies on the use of hierarchical proxies as learnable ancestors of the embedded data points in hyperbolic space. Given a triplet of points x_i, x_j, x_k where x_i and x_j are determined to be related by a reciprocal nearest neighbor measure, and x_k is an unrelated point, the HIER loss regularizer is then calculated as

$$\begin{aligned} \mathcal{L}_{\text{HIER}}(t) = & [D_B(x_i, \rho_{ij}) - D_B(x_i, \rho_{ijk}) + \delta]_+ \\ & + [D_B(x_j, \rho_{ij}) - D_B(x_j, \rho_{ijk}) + \delta]_+ \\ & + [D_B(x_k, \rho_{ijk}) - D_B(x_k, \rho_{ij}) + \delta]_+, \end{aligned} \quad (5)$$

where D_B denotes the hyperbolic distance on the Poincaré ball, and ρ_{ij} is the most likely least common ancestor of points x_i and x_j . This encourages a smaller hyperbolic distance between x_i, x_j , and ρ_{ij} , and a larger distance with ρ_{ijk} . The opposite signal is then applied in the case of x_k ,

the irrelevant data point. Kim et al. (2023) show substantial performance uplifts for the HIER loss when applied to a variety of network architectures.

In the following experiment, we extend HIER to the Lorentz model (LHIER) and compare against the results provided by Kim et al. (2023).

Moving to Lorentz Space To adapt the HIER model to the hyperboloid, we first replace the Euclidean layer norm and linear layer with a Lorentzian norm and linear layer (Bdeir et al., 2024). We then modify the HIER loss by setting the hierarchical proxies as learnable hyperbolic parameters and replace the Poincaré distance with the Lorentzian distance. This allows us to optimize the hyperbolic parameters directly on the manifold using our new optimization schema. We also apply distance rescaling before layer norm and after the linear layer. We refer to this setup as *LHIER*.

Experimental Goals Kim et al. (2023) employ the Euclidean AdamW optimizer with Euclidean parameterizations of hyperbolic proxies. Their experiments use FP16 precision. As the setting is already hyperbolic, significant gains from transitioning to Lorentz space are unlikely. We use this setup to evaluate our components’ ability to learn curvature in low-precision, unstable environments. Any improvements likely stem from better curvature adaptation to the data and task.

Experimental Setup We follow the experimental setup in Kim et al. (2023) and rely on four main datasets: CUB-200-2011 (CUB)(Welinder et al., 2010), Cars-196 (Cars)(Krause et al., 2013), Stanford Online Product (SOP)(Song et al., 2016), and In-shop Clothes Retrieval (InShop)(Liu et al., 2016). Performance is measured using Recall@k, the fraction of queries with at least one relevant sample in their k-nearest neighbors. All model backbones are pre-trained on ImageNet for fair comparisons.

Results As shown in Table 1, LHIER learns curvature without stability issues. Our approach improves model performance, with recall@1 gains ranging from 1.49% to 4.71%. Additional ablation experiments with different optimizers and configurations are detailed in Table 7.

4.2. EEG Classification Problem

Problem Setting Given EEG recordings labeled into distinct categories, the goal is to classify new recordings based on signal patterns. Each recording is a time series $X \in \mathbb{R}^{C \times T}$, where C is the number of channels and T is the time length. Each label is $y \in \{1, \dots, K\}$. Given N labeled recordings $(X_1, y_1), \dots, (X_N, y_N)$ from an unknown distribution p , the task is to train a model \hat{y} that maps EEG signals X to their correct class.

Table 1: Performance of metric learning methods on the four datasets as provided by (Kim et al., 2023). All architecture backbones are pretrained and tested with the new LHIER loss. Superscripts denote their embedding dimensions and † indicates models using larger input images. As in (Kim et al., 2023), network architectures are abbreviated as, R-ResNet50 (Wang et al., 2017), B-Inception with Batch-Norm (Ioffe & Szegedy, 2015), De-DeiT (Touvron et al., 2021), DN-DINO (Caron et al., 2021) and V-ViT (Dosovitskiy et al., 2020)

Methods	Arch.	CUB		Cars		SOP	
		R@1	R@2	R@1	R@2	R@1	R@10
<i>CNN Backbone</i>							
NSoftmax	R ¹²⁸	56.5	69.6	81.6	88.7	75.2	88.7
MIC	R ¹²⁸	66.1	76.8	82.6	89.1	77.2	89.4
XBM	R ¹²⁸	-	-	-	-	80.6	91.6
XBM	B ⁵¹²	65.8	75.9	82.0	88.7	79.5	90.8
HTL	B ⁵¹²	57.1	68.8	81.4	88.0	74.8	88.3
MS	B ⁵¹²	65.7	77.0	84.1	90.4	78.2	90.5
SoftTriple	B ⁵¹²	65.4	76.4	84.5	90.7	78.6	86.6
PA	B ⁵¹²	68.4	79.2	86.1	91.7	79.1	90.8
NSoftmax	R ⁵¹²	61.3	73.9	84.2	90.4	78.2	90.6
†ProxyNCA++	R ⁵¹²	69.0	79.8	86.5	92.5	<u>80.7</u>	<u>92.0</u>
Hyp	R ⁵¹²	65.5	76.2	81.9	88.8	79.9	91.5
HIER	R ⁵¹²	<u>70.1</u>	<u>79.4</u>	<u>88.2</u>	<u>93.0</u>	80.2	91.5
LHIER	R ⁵¹²	73.4	82.4	90.0	94.0	81.9	93.1
Increase %		4.71	3.78	2.04	1.08	1.49	1.20

Reference Model The reference model MAtt (Pan et al., 2022) has already taken steps towards improving data preparation. In the feature extraction phase, MAtt uses 2 convolutions along the time and sensor dimensions respectively. The embeddings are transformed into Symmetric Positive Definite (SPD) data by mapping the feature embeddings from Euclidean space onto the SPD manifold. The resulting sequence is then fed into a Manifold Attention Model and the outputs are projected back to the Euclidean space and classified using a fully connected layer.

Moving to Lorentz Space To adapt MAtt to a Lorentz space setting, we project the embeddings from the SPD manifold to the Lorentz manifold after the input slicing and sample covariance matrix projection. We then pass them through an adapted Lorentz Attention layer that replaces the SPD layers, distance function, and centroid with the Lorentzian counterparts. Finally, we use the Lorentz MLR (Bdeir et al., 2024) as a final classification head. We refer to this enhanced model as *HyperMAtt*.

Experimental Goals While this process already represents EEG sequences in Riemannian space, we enhance it further with our Riemannian AdamW Optimizer. Hyperbolic spaces are prone to overfitting, especially in EEG classification, where models are trained per subject with

limited sessions, leading to data scarcity. The proposed optimizer improves regularization, ensuring smoother and more balanced convergence. We avoid curvature learning, as it could worsen overfitting and reduce performance, but retain distance rescaling functions.

Experimental Setup We compare our model *HyperMAtt* on three common EEG datasets for the domain of EEG classification. These datasets are *MI* (Motor Imagery) (Brunner et al., 2008), *SSVEP* (Steady-State Visual Evoked Potentials) (Nikolopoulos, 2021) and *ERN* (Error-Related Negativity) (Margaux et al., 2012) representing three different tasks, motor imagery, visual stimuli, and error recognition, respectively. Here, we follow the same preprocessing procedure and train/val/test splits as MAtt. For the datasets MI and SSVEP, we use Accuracy as an evaluation metric and AUC.

For the application domain of EEG, we evaluate our method against current state-of-the-art models for EEG Classification including Inception (Burchert et al., 2024), MAtt (Pan et al., 2022), MBEEGSE (Altuwaijri et al., 2022), FBCNet (Mane et al., 2021), TCNet-Fusion (Musallam et al., 2021), EEG-TCNet (Ingolfsson et al., 2020), SCCNet (Wei et al., 2019), EEGNet (Lawhern et al., 2018), and ShallowConvNet (Schirrneister et al., 2017).

Results In Table 2 we show the performance of *HyperMAtt* compared to the current state-of-the-art baselines, where the results were aggregated from (Pan et al., 2022; Burchert et al., 2024). The performance for *HyperMAtt* is measured across 3 runs and we report the mean and standard deviation. Here, our new optimizer archives state-of-the-art results for SSVEP and ERN, the two comparatively smaller datasets, which are more prone to overfitting. We also show the improved performance of our RAdamW optimizer vs the existing RAdam by training the model using both and comparing the results in Table 8. We also achieve these results in significantly less time/epoch compared to MAtt. Specifically for MI 0.077s/epoch vs 3.4s/epoch, for SSVEP 0.081s/epoch vs 4s/epochs, and for ERN 0.061s/epoch vs 1.9s/epoch.

4.3. Standard Image Classification Problem

Problem Setting and Reference Model In their work, Bdeir et al. (2024) proposed a fully hyperbolic 2D convolutional layer by breaking down the convolution operation into a window-unfolding step followed by a modified version of the Lorentz Linear Layer from Chen et al. (2022). This approach ensured that the convolution outputs remained on the hyperboloid. However, the manual patch creation combined with matrix multiplication made the computation extremely expensive, as it prevented the use of highly optimized CUDA implementations for convolutions. As such, the authors proposed a two versions of their hyperbolic

Table 2: Performance comparison for the EEG datasets MI, SSVEP, and ERN. We report the average accuracy for MI and SSVEP and the AUC for ERN. The best result is highlighted in bold.

MODELS	MI	SSVEP	ERN
SHALLOWCONVNET	61.84±6.39	56.93±6.97	71.86±2.64
EEGNET	57.43±6.25	53.72±7.23	74.28±2.47
SCCNET	71.95±5.05	62.11±7.70	70.93±2.31
EEG-TCNET	67.09±4.66	55.45±7.66	77.05±2.46
TCNET-FUSION	56.52±3.07	45.00±6.45	70.46±2.94
FBCNET	71.45±4.45	53.09±5.67	60.47±3.06
MBEEGSE	64.58±6.07	56.45±7.27	75.46±2.34
INCEPTION	62.85±3.21	62.71±2.95	73.55±5.08
MATT	74.71±5.01	65.50±8.20	76.01±2.28
HYPERMATT (OURS)	74.12±2.91	68.10±2.41	78.01±1.30
INCREASE IN %	-0.79	3.97	1.25

ResNet classifier. A fully hyperbolic model with all Lorentz ResNet blocks (HCNN) and a hybrid encoder model with alternating Euclidean and hyperbolic blocks (HECNN).

Reference Optimization To adapt our methods for both models, we introduce the distance rescaling function after every convolution in the encoder. Additionally, we attempt to improve the performance by performing a parametrization trick on existing CUDA convolutions to ensure hyperbolic outputs. This is done by parametrizing the convolution weight as a rotation operation before passing the input, and then applying a boost operation afterwards. The end result is then equivalent to the convolution operation by Bdeir et al. (2024) while mitigating computation complexity. Specific implementation details can be found in Appendix B. We denote our Hybrid and Fully hyperbolic models as HECNN+ and HCNN+ respectively.

Experimental Goals In their paper, (Bdeir et al., 2024) notice lower performance in the fully hyperbolic models compared to the hybrid models and attribute this to instability in training. Additionally, they cite crashes and model divergence when learning the curvature instead of setting it to constant. This would then be an ideal setting to test the optimization schema and rescaling function and their impact on performance and stability. We do not use the RAdamW optimizer in this setting as RSGD is already used and employs proper L2-regularization.

Experimental Setup We follow the experimental setup and hyperparameters of Bdeir et al. (2024) and rely on three main datasets: CIFAR10, CIFAR100, and Mini-Imagenet. For ResNet-18, we employ HECNN+, following the structure outlined in Bdeir et al. (2024) with alternating Euclidean and hyperbolic blocks, and integrate our efficient convolution operation. We decouple the encoder and decoder manifolds, allowing each to independently learn its own curvature for enhanced model flexibility. We also imple-

ment ResNet-50 models of the proposed hyperbolic hybrid architectures using similarly constructed bottleneck blocks.

Results For the ResNet-18 experiments, Table 3 shows that the new models are able to remain stable while learning the curvature. Additionally, we see significant performance improvements between HCNN and HCNN+, where our proposed architecture now matches the performance of the hybrid encoders. We hypothesize that the improved scaling function helps mitigate the previous performance inconsistencies. However, the performance difference between the hybrid models is not significant, we hypothesize this is due to the alternating architecture which could limit the effect and instability of hyperbolic components. Finally, both models manage to maintain performance while reducing the memory footprint and runtime by approximately 25 – 50% and 18 – 25% respectively. One other benefit that we find from learning the curvature is quicker convergence where the model is able to reach convergence in 130 epochs vs the 200 epochs required by a static curve model.

Table 3: Runtime Analysis for the ResNet-18 models. We report classification accuracy (%) and estimate the mean and standard deviation from five runs. The best performance is highlighted in bold (higher is better).

	CIFAR-100 ($\delta_{rel} = 0.23$)	VRAM/ t_{epoch} For Cifar100	Tiny-ImageNet ($\delta_{rel} = 0.20$)
Euclidean	77.72 \pm 0.15	1.2GB - 12s	65.19 \pm 0.12
Hybrid (\mathbb{P})	77.19 \pm 0.50	-	64.93 \pm 0.38
Hybrid (\mathbb{L})	78.03 \pm 0.21	-	65.63 \pm 0.10
ResNet (\mathbb{P})	76.60 \pm 0.32	-	62.01 \pm 0.56
HECNN (\mathbb{L})	78.76 \pm 0.24	4.3GB - 100s	65.96 \pm 0.18
HECNN+	78.80 \pm 0.12	3GB - 80s	65.98 \pm 0.11
HCNN (\mathbb{L})	78.07 \pm 0.17	10GB - 175s	65.71 \pm 0.13
HCNN+	78.81\pm0.19	5GB - 140s	66.12\pm0.14

In the ResNet-50 experiments in Table 4, HECNN+ significantly outperforms both the Euclidean model and the base hybrid model across both datasets. We also see a $\sim 48\%$ reduction in memory usage and $\sim 66\%$ reduction in runtime. We attribute this improvement to efficient closed-source convolution operations we can now leverage.

Table 4: Runtime Analysis for ResNet-50 models. We report classification accuracy (%) and the best performance is highlighted in bold (higher is better).

	CIFAR-100 ($\delta_{rel} = 0.23$)	VRAM/ t_{epoch}	Tiny-ImageNet ($\delta_{rel} = 0.20$)
Euclid	78.52	4.5GB - 30s	66.23
HECNN	79.83	15.6GB - 300s	66.30
HECNN+	80.86	8.1GB - 100s	67.18

Table 5: Reconstruction and generation FID of manifold VAEs across five runs (lower is better).

	CIFAR-100		CELEBA	
	REC. FID	GEN. FID	REC. FID	GEN. FID
EUCLID	63.81 \pm 0.47	103.54 \pm 0.84	54.80 \pm 0.29	79.25 \pm 0.89
HYBRID (\mathbb{P})	62.64 \pm 0.43	98.19 \pm 0.57	54.62 \pm 0.61	81.30 \pm 0.56
HYBRID (\mathbb{L})	62.14 \pm 0.35	98.34 \pm 0.62	54.64 \pm 0.34	82.78 \pm 0.93
HCNN (\mathbb{L})	61.44 \pm 0.64	100.27 \pm 0.84	54.17 \pm 0.66	78.11 \pm 0.95
HCNN+ (\mathbb{L})	57.69\pm0.52	98.14\pm0.44	52.73\pm0.27	77.98\pm0.32
DECREASE IN %	6.10	2.12	2.66	0.17

4.4. VAE Image Generation

Problem Setting and Reference Model Previous research has highlighted the ability of hyperbolic neural networks to perform better when using lower dimensional embeddings due to the more expressive space (Nagano et al., 2019; Mathieu et al., 2019; Ovinnikov, 2019; Hsu et al., 2020). A natural extension to this would be implementing the models for VAEs which rely on smaller latent embedding dimensions to encode the inputs. Bdeir et al. (2024) perform this study on image generation and reconstruction for their fully hyperbolic models.

Experimental Setup We reproduce the experimental setup from (Bdeir et al., 2024) and re-implement the fully hyperbolic VAE using our new efficient convolution and transpose convolution layers. We also use curvature learning with our adjusted Riemannian SGD learning scheme.

Results Our fully hyperbolic VAE implementation outperforms on both datasets, as shown in Table 5, while using 2.5x less memory and training 3x faster. This highlights the effectiveness of our curvature learning process and efficient model components.

5. Conclusion

In this work, we propose a robust curvature-aware optimization framework for hyperbolic deep learning, addressing challenges in stability, computational efficiency, and overfitting. By introducing Riemannian AdamW, a novel distance rescaling function, and leveraging efficient CUDA implementations, our approach achieved performance improvements in hierarchical metric learning, EEG classification, and image classification tasks, while reducing computational costs, highlighting the practicality of our methods for large-scale applications. These findings emphasize the importance of proper curvature adaptation in hyperbolic learning, paving the way for future research in optimizing hyperbolic embeddings across diverse fields.

6. Impact Statement

This paper presents work whose goal is to advance the field of Machine Learning. We are committed to contributing positively to society and human well-being, while respecting the privacy of the subjects involved in our evaluation. Our experiments utilize three established EEG datasets: MI, SSVEP, and ERN, which involve data from human subjects. These datasets are fully anonymized and do not contain any personally identifiable information. Additionally, they are publicly available and widely used within the machine learning community.

References

- Altuwaijri, G. A., Muhammad, G., Altaheri, H., and Al-sulaiman, M. A multi-branch convolutional neural network with squeeze-and-excitation attention blocks for eeg-based motor imagery signals classification. *Diagnostics*, 12(4):995, 2022.
- Atigh, M. G., Schoep, J., Acar, E., van Noord, N., and Mettes, P. Hyperbolic image segmentation. In *Proceedings of the IEEE/CVF Conference on Computer Vision and Pattern Recognition (CVPR)*, pp. 4453–4462, June 2022.
- Bdeir, A., Schwethelm, K., and Landwehr, N. Fully hyperbolic convolutional neural networks for computer vision, 2024.
- Brunner, C., Leeb, R., Müller-Putz, G., Schlögl, A., and Pfurtscheller, G. Bci competition 2008–graz data set a. *Institute for Knowledge Discovery (Laboratory of Brain-Computer Interfaces)*, Graz University of Technology, 16: 1–6, 2008.
- Burchert, J., Werner, T., Yalavarthi, V. K., de Portugal, D. C., Stubbemann, M., and Schmidt-Thieme, L. Are eeg sequences time series? eeg classification with time series models and joint subject training. *arXiv preprint arXiv:2404.06966*, 2024.
- Caron, M., Touvron, H., Misra, I., Jégou, H., Mairal, J., Bojanowski, P., and Joulin, A. Emerging properties in self-supervised vision transformers. In *Proc. IEEE International Conference on Computer Vision (ICCV)*, 2021.
- Chen, W., Han, X., Lin, Y., Zhao, H., Liu, Z., Li, P., Sun, M., and Zhou, J. Fully hyperbolic neural networks, 2022.
- Dai, J., Wu, Y., Gao, Z., and Jia, Y. A hyperbolic-to-hyperbolic graph convolutional network, 2021.
- Dhingra, B., Shallue, C. J., Norouzi, M., Dai, A. M., and Dahl, G. E. Embedding text in hyperbolic spaces, 2018.
- Dosovitskiy, A., Beyer, L., Kolesnikov, A., Weissenborn, D., Zhai, X., Unterthiner, T., Dehghani, M., Minderer, M., Heigold, G., Gelly, S., et al. An image is worth 16x16 words: Transformers for image recognition at scale. *arXiv preprint arXiv:2010.11929*, 2020.
- Ganea, O., Becigneul, G., and Hofmann, T. Hyperbolic neural networks. In Bengio, S., Wallach, H., Larochelle, H., Grauman, K., Cesa-Bianchi, N., and Garnett, R. (eds.), *Advances in Neural Information Processing Systems*, volume 31. Curran Associates, Inc., 2018. URL <https://proceedings.neurips.cc/paper/2018/file/dbab2adc8f9d078009ee3fa810bea142-Paper.pdf>.
- Gao, Z., Wu, Y., Jia, Y., and Harandi, M. Hyperbolic feature augmentation via distribution estimation and infinite sampling on manifolds. *Advances in neural information processing systems*, 35:34421–34435, 2022.
- Giovanni, F. D., Luise, G., and Bronstein, M. Heterogeneous manifolds for curvature-aware graph embedding, 2022.
- Gu, A., Sala, F., Gunel, B., and Ré, C. Learning mixed-curvature representations in product spaces. In *International Conference on Learning Representations*, 2018. URL <https://api.semanticscholar.org/CorpusID:108328651>.
- Guo, Y., Wang, X., Chen, Y., and Yu, S. X. Clipped hyperbolic classifiers are super-hyperbolic classifiers. In *2022 IEEE/CVF Conference on Computer Vision and Pattern Recognition (CVPR)*, pp. 1–10, Los Alamitos, CA, USA, jun 2022. IEEE Computer Society. doi: 10.1109/CVPR52688.2022.00010. URL <https://doi.ieeecomputersociety.org/10.1109/CVPR52688.2022.00010>.
- Hsu, J., Gu, J., Wu, G.-H., Chiu, W., and Yeung, S. Capturing implicit hierarchical structure in 3d biomedical images with self-supervised hyperbolic representations, 2020. URL <https://arxiv.org/abs/2012.01644>.
- Ingolfsson, T. M., Hersche, M., Wang, X., Kobayashi, N., Cavigelli, L., and Benini, L. Eeg-tcnnet: An accurate temporal convolutional network for embedded motor-imagery brain–machine interfaces. In *2020 IEEE International Conference on Systems, Man, and Cybernetics (SMC)*, pp. 2958–2965. IEEE, 2020.
- Ioffe, S. and Szegedy, C. Batch normalization: Accelerating deep network training by reducing internal covariate shift. In *Proc. International Conference on Machine Learning (ICML)*, 2015.

- Khrulkov, V., Mirvakhabova, L., Ustinova, E., Oseledets, I., and Lempitsky, V. Hyperbolic image embeddings. In *Proc. IEEE Conference on Computer Vision and Pattern Recognition (CVPR)*, 2020.
- Kim, S., Jeong, B., and Kwak, S. Hier: Metric learning beyond class labels via hierarchical regularization, 2023.
- Kochurov, M., Karimov, R., and Kozlukov, S. Geopt: Riemannian optimization in pytorch, 2020.
- Krause, J., Stark, M., Deng, J., and Fei-Fei, L. 3d object representations for fine-grained categorization. In *Proceedings of the IEEE International Conference on Computer Vision Workshops*, pp. 554–561, 2013.
- Law, M., Liao, R., Snell, J., and Zemel, R. Lorentzian distance learning for hyperbolic representations. In Chaudhuri, K. and Salakhutdinov, R. (eds.), *Proceedings of the 36th International Conference on Machine Learning*, volume 97 of *Proceedings of Machine Learning Research*, pp. 3672–3681. PMLR, 09–15 Jun 2019. URL <https://proceedings.mlr.press/v97/law19a.html>.
- Lawhern, V. J., Solon, A. J., Waytowich, N. R., Gordon, S. M., Hung, C. P., and Lance, B. J. Eegnet: a compact convolutional neural network for eeg-based brain-computer interfaces. *Journal of Neural Engineering*, 15(5):056013, 2018.
- Liu, S., Qi, X., Shi, J., Zhang, H., and Jia, J. Multi-scale patch aggregation (MPA) for simultaneous detection and segmentation. In *Proc. IEEE Conference on Computer Vision and Pattern Recognition (CVPR)*, 2016.
- Liu, S., Chen, J., Pan, L., Ngo, C.-W., Chua, T.-S., and Jiang, Y.-G. Hyperbolic visual embedding learning for zero-shot recognition. In *2020 IEEE/CVF Conference on Computer Vision and Pattern Recognition (CVPR)*, pp. 9270–9278, 2020. doi: 10.1109/CVPR42600.2020.00929.
- Loshchilov, I. and Hutter, F. Decoupled weight decay regularization, 2019.
- Mane, R., Chew, E., Chua, K., Ang, K. K., Robinson, N., Vinod, A. P., Lee, S.-W., and Guan, C. Fbcnet: A multi-view convolutional neural network for brain-computer interface. *arXiv preprint arXiv:2104.01233*, 2021.
- Margaux, P., Emmanuel, M., Sébastien, D., Olivier, B., and Jérémie, M. Objective and subjective evaluation of online error correction during p300-based spelling. *Advances in Human-Computer Interaction*, 2012:4–4, 2012.
- Mathieu, E., Lan, C. L., Maddison, C. J., Tomioka, R., and Teh, Y. W. Continuous hierarchical representations with poincaré variational auto-encoders, 2019. URL <https://arxiv.org/abs/1901.06033>.
- Mettes, P., Atigh, M. G., Keller-Ressel, M., Gu, J., and Yeung, S. Hyperbolic deep learning in computer vision: A survey, 2023.
- Mishne, G., Wan, Z., Wang, Y., and Yang, S. The numerical stability of hyperbolic representation learning, 2022. URL <https://arxiv.org/abs/2211.00181>.
- Moretti, V. The interplay of the polar decomposition theorem and the lorentz group, 2002. URL <https://arxiv.org/abs/math-ph/0211047>.
- Musallam, Y. K., AlFassam, N. I., Muhammad, G., Amin, S. U., Alsulaiman, M., Abdul, W., Altaheri, H., Bencherif, M. A., and Algabri, M. Electroencephalography-based motor imagery classification using temporal convolutional network fusion. *Biomedical Signal Processing and Control*, 69:102826, 2021.
- Nagano, Y., Yamaguchi, S., Fujita, Y., and Koyama, M. A wrapped normal distribution on hyperbolic space for gradient-based learning, 2019. URL <https://arxiv.org/abs/1902.02992>.
- Nikolopoulos, S. Mamem eeg ssvep dataset ii (256 channels, 11 subjects, 5 frequencies presented simultaneously). 2021.
- Ovinnikov, I. Poincaré wasserstein autoencoder. 2019. doi: 10.48550/ARXIV.1901.01427. URL <https://arxiv.org/abs/1901.01427>.
- Pan, Y.-T., Chou, J.-L., and Wei, C.-S. Matt: A manifold attention network for eeg decoding. *Advances in Neural Information Processing Systems*, 35:31116–31129, 2022.
- Peng, W., Varanka, T., Mostafa, A., Shi, H., and Zhao, G. Hyperbolic deep neural networks: A survey. *IEEE Transactions on Pattern Analysis and Machine Intelligence*, 44(12):10023–10044, 2022. doi: 10.1109/TPAMI.2021.3136921.
- Qu, E. and Zou, D. Lorentzian fully hyperbolic generative adversarial network, 2022. URL <https://arxiv.org/abs/2201.12825>.
- Qu, E. and Zou, D. Hyperbolic convolution via kernel point aggregation, 2023.
- Schirrmeister, R. T., Springenberg, J. T., Fiederer, L. D. J., Glasstetter, M., Eggenberger, K., Tangermann, M., Hutter, F., Burgard, W., and Ball, T. Deep learning with convolutional neural networks for eeg decoding and visualization. *Human Brain Mapping*, 38(11):5391–5420, 2017.
- Song, H. O., Xiang, Y., Jegelka, S., and Savarese, S. Deep metric learning via lifted structured feature embedding. In

Proc. IEEE Conference on Computer Vision and Pattern Recognition (CVPR), 2016.

Tifrea, A., Bécigneul, G., and Ganea, O.-E. Poincaré glove: Hyperbolic word embeddings, 2018.

Touvron, H., Cord, M., Douze, M., Massa, F., Sablayrolles, A., and Jégou, H. Training data-efficient image transformers & distillation through attention. In *Proc. International Conference on Machine Learning (ICML)*, 2021.

van Spengler, M., Berkhout, E., and Mettes, P. Poincaré resnet, 2023.

Wang, Z., Yan, W., and Oates, T. Time series classification from scratch with deep neural networks: A strong baseline. In *2017 International Joint Conference on Neural Networks (IJCNN)*, pp. 1578–1585. IEEE, 2017.

Wei, C.-S., Koike-Akino, T., and Wang, Y. Spatial component-wise convolutional network (sccnet) for motor-imagery eeg classification. In *2019 9th International IEEE/EMBS Conference on Neural Engineering (NER)*, pp. 328–331. IEEE, 2019.

Welinder, P., Branson, S., Mita, T., Wah, C., Schroff, F., Belongie, S., and Perona, P. Caltech-UCSD Birds 200. Technical Report CNS-TR-2010-001, California Institute of Technology, 2010.

Yang, M., Zhou, M., Ying, R., Chen, Y., and King, I. Hyperbolic representation learning: Revisiting and advancing, 2023. URL <https://arxiv.org/abs/2306.09118>.

Zhu, Y., Zhou, D., Xiao, J., Jiang, X., Chen, X., and Liu, Q. Hypertext: Endowing fasttext with hyperbolic geometry, 2021.

A. Operations in hyperbolic geometry

Parallel Transport A parallel transport operation $\text{PT}_{\mathbf{x} \rightarrow \mathbf{y}}^K(\mathbf{v})$ describes the mapping of a vector on the manifold \mathbf{v} from the tangent space of $\mathbf{x} \in \mathbb{L}$ to the tangent space of $\mathbf{y} \in \mathbb{L}$. This operation is given as $\text{PT}_{\mathbf{x} \rightarrow \mathbf{y}}^K(\mathbf{v}) = \mathbf{v} + \frac{\langle \mathbf{y}, \mathbf{v} \rangle_{\mathbb{L}}}{K - \langle \mathbf{x}, \mathbf{y} \rangle_{\mathbb{L}}}(\mathbf{x} + \mathbf{y})$.

Lorentzian Centroid (Law et al., 2019) Also denoted as $\mu_{\mathbb{L}}$, is the weighted centroid between points on the manifold based on the Lorentzian square distance. Given the weights $\nu, \mu = \frac{\sum_{i=1}^m \nu_i \mathbf{x}_i}{\sqrt{1/K} \|\sum_{i=1}^m \nu_i \mathbf{x}_i\|_{\mathbb{L}}}$.

Lorentz Transformations In the Lorentz model, linear transformations preserving the structure of spacetime are termed Lorentz transformations. A matrix $\mathbf{A}^{(n+1) \times (n+1)}$ is defined as a Lorentz transformation if it provides a linear mapping from \mathbb{R}^{n+1} to \mathbb{R}^{n+1} that preserves the inner product, i.e., $\langle \mathbf{A}\mathbf{x}, \mathbf{A}\mathbf{y} \rangle_{\mathbb{L}} = \langle \mathbf{x}, \mathbf{y} \rangle_{\mathbb{L}}$ for all $\mathbf{x}, \mathbf{y} \in \mathbb{R}^{n+1}$. The collection of these matrices forms an orthogonal group, denoted $\mathbf{O}(1, n)$, which is commonly referred to as the Lorentz group.

In this model, we restrict attention to transformations that preserve the positive time orientation, operating within the upper sheet of the two-sheeted hyperboloid. Accordingly, the transformations we consider lie within the positive Lorentz group, denoted $\mathbf{O}^+(1, n) = \mathbf{A} \in \mathbf{O}(1, n) : a_{11} > 0$, ensuring preservation of the time component sign x_t for any $\mathbf{x} \in \mathbb{L}_K^n$. Specifically, in this context, Lorentz transformations satisfy the relation

$$\mathbf{O}^+(1, n) = \mathbf{A} \in \mathbb{R}^{(n+1) \times (n+1)} | \forall \mathbf{x} \in \mathbb{L}_K^n : \langle \mathbf{A}\mathbf{x}, \mathbf{A}\mathbf{x} \rangle_{\mathbb{L}} = -\frac{1}{K}, (\mathbf{A}\mathbf{x})_0 > 0. \quad (6)$$

Each Lorentz transformation can be decomposed via polar decomposition into a Lorentz rotation and a Lorentz boost, expressed as $\mathbf{A} = \mathbf{R}\mathbf{B}$ (Moretti, 2002). The rotation matrix \mathbf{R} is designed to rotate points around the time axis and is defined as

$$\mathbf{R} = \begin{bmatrix} 1 & \mathbf{0}^T \\ \mathbf{0} & \tilde{\mathbf{R}} \end{bmatrix}, \quad (7)$$

where $\mathbf{0}$ represents a zero vector, $\tilde{\mathbf{R}}$ satisfies $\tilde{\mathbf{R}}^T \tilde{\mathbf{R}} = \mathbf{I}$, and $\det(\tilde{\mathbf{R}}) = 1$. This structure shows that Lorentz rotations on the upper hyperboloid sheet belong to a special orthogonal subgroup, $\mathbf{SO}^+(1, n)$, which preserves orientation, with $\tilde{\mathbf{R}} \in \mathbf{SO}(n)$.

In contrast, the Lorentz boost applies shifts along spatial axes given a velocity vector $\mathbf{v} \in \mathbb{R}^n$ with $\|\mathbf{v}\| < 1$, without altering the time axis.

$$\mathbf{B} = \begin{bmatrix} \gamma & -\gamma \mathbf{v}^T \\ -\gamma \mathbf{v} & \mathbf{I} + \frac{\gamma^2}{1+\gamma} \mathbf{v} \mathbf{v}^T \end{bmatrix}, \quad (8)$$

with $\gamma = \frac{1}{\sqrt{1-\|\mathbf{v}\|^2}}$. However, this can also be any operation that scales the norms of the space values without changing the vector orientation.

B. Convolution Trick

To address the computational requirements issue, we adopt an alternative definition of the Lorentz Linear layer from Dai et al. (2021), which decomposes the transformation into a Lorentz boost and a Lorentz rotation. Using this definition, we replace the matrix multiplication employed by Bdeir et al. (2024) for the spatial dimensions and time component projection with a learned rotation operation and a Lorentz boost. Additionally, we can achieve the rotation operation using a parameterization of the convolution weights while still relying on the CUDA convolution implementations, significantly improving computational efficiency.

To apply this concept to the convolution operation, the convolution weights, after unfolding, must form a rotation matrix. We define the dimensions of this matrix as $n = (\text{channels}_{in} \cdot \text{kernel}_{width} \cdot \text{kernel}_{height})$ and $n' = \text{channels}_{out}$ respectively. We then use either rotation operation presented above to a norm-preserving transformation $\mathbf{z} = \mathbf{W}^T \mathbf{x} \cdot \frac{\|\mathbf{x}\|}{\|\mathbf{W}^T \mathbf{x}\|}$ where $\mathbf{W} \in \mathbb{R}^{(n' \cdot n)}$. This formulation allows us to utilize existing efficient implementations of the convolution operation by

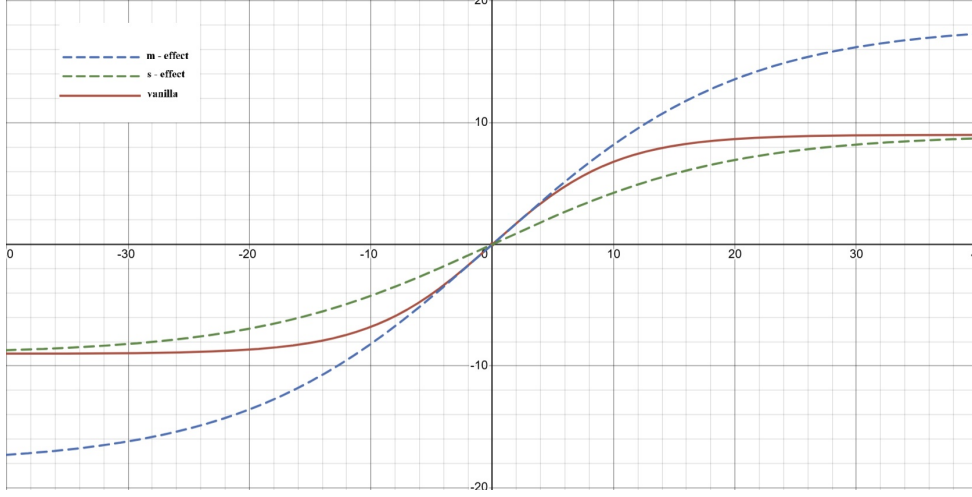


Figure 2: The output of the proposed flexible tanh function. Here the maximum value m is set to 9.1 in the vanilla version with an alternate value of $m=18$ and the slope s is set to 2.6 with an alternate value of 3.5

directly parameterizing the kernel weights before passing them into the convolutional layer. Finally, we formalize the new Lorentz Convolution as:

$$\mathit{out} = \text{LorentzBoost}(\text{DistanceRescaling}(\text{RotationConvolution}(x))) \quad (9)$$

where TanhRescaling is the operation described in Eq.4 and $\text{RotationConvolution}$ is a normal convolution parameterized through the procedure in Algorithm 2 where Transform is the norm-preserving transformation above.

Algorithm 2 Lorentz Convolution Parametarization

```

 $\mathbf{W} \in \mathbb{R}^{C_{in}, C_{out}, K_{width}, K_{length}}$ 
function Adaptweight
  if  $K_{width} \cdot K_{length} \cdot C_{in} > C_{out}$  then
    return  $\mathbf{W}$ 
  else
     $\mathbf{W} = \mathbf{W}.\text{reshape}(K_{width} \cdot K_{length} \cdot C_{in}, C_{out})$ 
     $\hat{\mathbf{W}}_{core} = \text{Transform}(\mathbf{W})$ 
    return  $\hat{\mathbf{W}}.\text{reshape}(C_{in}, C_{out}, K_{width}, K_{length})$ 
  end if
end function
    
```

C. Scaling Lorentzian Vectors

Tanh Scaling We show the output of the tanh scaling function in Figure 2. By changing the transformation parameters we are able to fine-tune the maximum output and the slope to match our desired function response.

Hyperbolic Scaling We isolate the transformation of the $\exp_0^K(y)$ operation on the space values of y as:

$$\mathbf{x}_s = \sqrt{K} \times \sinh\left(\frac{\|\mathbf{y}\|_{\mathbb{L}}}{\sqrt{K}}\right) \frac{\mathbf{y}}{\|\mathbf{y}\|_{\mathbb{L}}} \quad (10)$$

where $\mathbf{y} \in \mathbb{R}^d = \log_0^K(x)$. However, at the tangent plane of the origin, the first element y_0 becomes 0. As such $\|\mathbf{y}\|_{\mathbb{L}} = \|\mathbf{y}\|_{\mathbb{E}} = \sum_{i=2}^d \mathbf{y}_i^2$. This gives us:

Table 7: Ablation on components for Metric Learning

Methods	Arch.	CUB		Cars		SOP	
		R@1	R@2	R@1	R@2	R@1	R@10
<i>CNN Backbone</i>							
LHIER RSGD	R ⁵¹²	64.2	72.1	73.9	81.4	67.8	73.9
LHIER RAdam	R ⁵¹²	70.1	79.8	87.6	92.0	79.8	90.3
LHIER CST Curvature	R ⁵¹²	71.2	80.8	88.7	91.8	79.1	89.7
LHIER No Learning Schema	R ⁵¹²	65.8	72.0	-	-	-	-
LHIER	R ⁵¹²	73.4	82.4	90.0	94.0	81.9	93.1

$$\mathbf{x}_s = \sqrt{K} \times \sinh\left(\frac{\|\mathbf{y}\|_{\mathbb{E}}}{\sqrt{K}}\right) \frac{\mathbf{y}}{\|\mathbf{y}\|_{\mathbb{E}}} \quad (11)$$

We can now scale the norm of the Euclidean vector \mathbf{y} by a value a and find the equivalent value for the hyperbolic space elements:

$$a_{\mathbb{L}} = \frac{\mathbf{x}_{s_{rescaled}}}{\mathbf{x}_s} = \frac{\sinh\left(\frac{a \times \|\mathbf{y}\|_{\mathbb{E}}}{\sqrt{K}}\right)}{\sinh\left(\frac{\|\mathbf{y}\|_{\mathbb{E}}}{\sqrt{K}}\right)} = \frac{e^{\frac{a \times \|\mathbf{y}\|_{\mathbb{E}}}{\sqrt{K}}} - e^{-\frac{a \times \|\mathbf{y}\|_{\mathbb{E}}}{\sqrt{K}}}}{e^{\frac{\|\mathbf{y}\|_{\mathbb{E}}}{\sqrt{K}}} - e^{-\frac{\|\mathbf{y}\|_{\mathbb{E}}}{\sqrt{K}}}} \quad (12)$$

Additionally, we know that the hyperbolic distance from the origin of the manifold to any point is equal to the norm of the projected vector onto the tangent plane. Supposing that we want $a \times D(\mathbf{x}, \bar{\mathbf{0}})^K = D(\mathbf{x}, \bar{\mathbf{0}})_{rescaled}^K$, we get the final equation:

$$\mathbf{x}_{s_{rescaled}} = \mathbf{x}_s \times \frac{e^{\frac{D(\mathbf{x}, \bar{\mathbf{0}})_{rescaled}^K}{\sqrt{K}}} - e^{-\frac{D(\mathbf{x}, \bar{\mathbf{0}})_{rescaled}^K}{\sqrt{K}}}}{e^{\frac{D(\mathbf{x}, \bar{\mathbf{0}})^K}{\sqrt{K}}} - e^{-\frac{D(\mathbf{x}, \bar{\mathbf{0}})^K}{\sqrt{K}}}} \quad (13)$$

D. Ablations

D.1. Image Classification

We test the effect of individual model components in Table 6. Each subsequent model involves the default architecture presented in the experimental setup minus the mentioned component. As we can see, the best results are achieved when all the architectural components are included. In the case of attempting to learn the curvature without the proposed optimizer schema, the model breaks completely down due to excessive numerical inaccuracies.

D.2. Metric Learning

In Table 7 we present the LHIER model results under different optimizers and components.

D.3. EEG Classification

We also train the model with the original Adam Optimizer and include the results in Table 8. This clearly shows the improvement provided by our RAdamW optimizer over standard RAdam.

Table 6: Ablation experiments for Resnet-50 models on Cifar-100.

	CIFAR-100
HCNN+ - Default	80.86
HCNN+ - fixed curve	79.6
HCNN+ - no scaling	80.13
HCNN+ - no optim scheme	<i>NaaN</i>

Table 8: Performance comparison for the EEG datasets MI, SSVEP, and ERN. We report the average accuracy for MI and SSVEP and the AUC for ERN. The best result is highlighted in bold.

MODELS	MI	SSVEP	ERN
HYPERMATT + ADAM (OURS)	68.53±1.29	62.42±2.62	74.98±5.84
HYPERMATT + ADAMW (OURS)	74.12±2.91	68.10±2.41	78.01±1.30